Chapter 5

The Role of Variations of the Earth's Orbital Characteristics in Climate Change

Lucas J. Lourens
Department of Earth Sciences, Faculty of Geosciences, Utrecht University, Budapestlaan 4, 3584 CD Utrecht, The Netherlands

Erik Tuenter
Institute for Marine and Atmospheric Research Utrecht (IMAU), P.O. Box 80 000, 3508 TA Utrecht, The Netherlands

1. INTRODUCTION

The climate of the Earth is characterised by trends, aberrations and quasi-periodic oscillations varying over a broad range of time-scales [1]. The trends are largely controlled by plate tectonics, and thus tend to change gradually on a million year (Ma) time scale. Aberrations occur when certain thresholds are passed and are manifested in the geological record as unusually rapid (less than a few thousand of years) or extreme changes in climate. The quasi-periodic oscillations are mostly astronomically paced; they are driven by astronomical perturbations that affect the Earth's orbit around the Sun and the orientation of the Earth's rotation axis with respect to its orbital plane. These perturbations are described by three main astronomical cycles: eccentricity (shape of the Earth's orbit), precession (date of perihelion) and obliquity (angle between the equator and orbital plane), which together

Climate Change: Observed Impacts on Planet Earth

determine the spatial and seasonal pattern of insolation received by the Earth, eventually resulting in climatic oscillations of tens to hundreds of thousands of years. The expression of these astronomical-induced climate oscillations is found in geological archives of widely different ages and environments.

Computation of the orbital solution of the Earth is complex because the Earth's motion is perturbed by our Moon and all the other planets of the Solar System. Much of our knowledge of the planetary orbits dates back to the investigations of Johannes Kepler (1571–1630) and the universal gravitational theory of Sir Isaac Newton (1643–1727). The first approximate solutions were established by Lagrange [2,3] and Pontécoulant [4], but it was Louis Agassiz [5], who formulated a sweeping theory of Ice Ages that triggered the search for a correlation between large-scale climatic changes and variations of the Earth's astronomical parameters. Shortly after, Adhémar [6] proposed that glaciations originated from the precession of the Earth's rotation axis that alters the lengths of the seasons. He suggested that when the lengths of the winters last longer a glaciation would occur. According to his theory, the Northern Hemisphere (NH) and the Southern Hemisphere (SH) would be glaciated during the opposing phases of the precession cycle. He evidenced his idea with the present Antarctic ice sheet and the fact that the NH is essentially not glaciated.

After the publication of a more precise solution of the Earth by Le Verrier [7], Croll [8] proposed that the variation of the Earth's eccentricity was also an important parameter for understanding past climates through its modulation of precession. He elaborated Adhémar's idea that winter insolation is critical for glaciation, but argued that the large continental areas covered with snow would turn into ice sheets because of a positive ice-albedo feedback.

The first computations of the variations of obliquity due to secular changes in the motion of the Earth's orbital plane are due to Pilgrim [9]. His computations were later used by Milankovitch [10] to establish his mathematical basis for the theory of the Ice Ages. Since then the understanding of the climate response to orbital forcing has evolved and is the subject of this chapter. However, all the necessary elements for the insolation computations were present in Milankovitch's work.

2. ASTRONOMICAL PARAMETERS

Bretagnon [11] made an important improvement to the orbital solution by computing terms of second order and third degree in the secular (mean) equations. His solution was used by Berger [12,13] for the computation of the precession and insolation quantities for the Earth following Sharav and Boudnikova [14,15]. Berger's publications have since been extensively used for paleoclimate reconstructions and climate modelling under the acronym Ber78.

Laskar [16–18] computed in an extensive way the secular equations giving the mean motion of the whole Solar System. It was clear from his computations that the traditional perturbation theory could not be used for the integration of the secular equations, due to strong divergences that became apparent in the system of the inner planets [16]. This difficulty was overcome by switching to a numerical integration of the secular equations with steps of 0.5 ka. These computations provided a much more accurate solution for the orbital motion of the Solar System over 10 Ma [18,19].

Extending his integration to 200 Ma, Laskar [20,21] demonstrated that the orbital motion of the planets, and especially that of the terrestrial planets, is chaotic, with an exponential divergence corresponding to an increase of the error by a factor 10 every 10 Ma. It seems, therefore, almost impossible to obtain a precise astronomical solution for paleoclimate studies over more than a few tens of millions of years [22].

A comparison between the La90 solution and the first direct numerical integration of the Solar System by Quinn and coworkers [23] revealed that the main obliquity and precession periods of the two solutions diverge with time over the past 3 Ma [24]. In the QTD91 solution, a term was introduced which describes the change in the speed of rotation of the Earth as a result of the dissipation of energy by the tides. If the same, present-day value is used in the La90 solution the discrepancy with QTD91 is almost completely removed. The resulting La90 solution with tidal dissipation set to the present-day value is now generally termed as the La93 solution. In this solution, also a second term can be modified. This term refers to the change in the dynamical ellipticity of the Earth, which may strongly depend on the build-up and retreat of large ice caps [25–28] and/or on long-term mantle convection processes [29]. Similar to the tidal dissipation term, a small change in the dynamical ellipticity of the Earth will change the main precession and obliquity frequencies.

The uncertain values of the tidal dissipation and dynamical ellipticity of the Earth are considered as the most limiting factors to obtain accurate solutions for the precession and obliquity time series of the Earth over a time span of millions of years, while the orbital part of the La93 solution was considered to be reliable over 10–20 Ma [24]. At present, there exists only one possible way to test the extent of change of both parameters in the (geological) past. This test involves a statistical comparison between the obliquity–precession interference patterns in the insolation time series and those observed in geological records [30]. Lourens and coworkers [31] showed for instance by using a record of climate change from the eastern Mediterranean, that over the past 3 Ma the decline in the speed of rotation was on average smaller than the average value obtained for the present day; this is probably a result of the large ice caps that dominated Earth's climate from the Late Pliocene to present.

In 2004, Laskar and coworkers [32] presented a new numerical solution from −250 to 250 Ma, which has been used for the direct calibration of the youngest geological period, the Neogene, spanning the last 23 Ma [33], and of the early Paleogene [34–36]. Beyond 40–50 Ma the chaotic evolution of the orbits still prevents a precise determination of the Earth motion. However, the most regular component of the orbital solution (i.e., the 405 ka period in eccentricity) could still be used over the last 250 Ma or full Mesozoic era.

2.1. Eccentricity

The Earth's orbit around the Sun is an ellipse. The plane in which the Earth moves around the Sun is called the Ecliptic of date, Ec_t (Fig. 1). The Sun is roughly located in one of its two foci. The eccentricity (e) of the Earth's orbit is defined as:

$$e = \frac{\sqrt{a^2 - b^2}}{a^2} \tag{1}$$

where a is the ellipse semi-major axis and b the semi-minor axis. The current eccentricity is 0.0167 but in the past hundred millions of years eccentricity has varied from about 0.0669 to almost 0.0001; that is, a near-circular orbit [32]. For the past 15 Ma, the three most important periods in the series expansion for eccentricity are about 405, 124 and 95 ka (Fig. 2e).

2.2. Precession and Obliquity

The locations along the Earth's orbit where the Sun is perpendicular to the equator at noon are called equinoxes (Fig. 1a). Then the night lasts as long as the day at all latitudes. Today this occurs on 20 March (vernal equinox, NH spring) and on 23 September (autumnal equinox, NH autumn). The summer (winter) solstice is defined as the location of the Earth when the Sun appears directly overhead at noon at its northernmost (southernmost) latitude, that is, the tropic of Cancer at 23.44°N (Capricorn at 23.44°S), which occurs on 21 June (22 December).

The Earth's rotational axis (φ) revolves around the normal (n) to the orbital plane like a spinning top (ψ in Fig. 1). This rotation causes a clockwise movement of the equinoxes and solstices along the Earth's orbit, called precession. The quasi-period of precession is 25 672 a relative to the stars, but because the Earth's orbit rotates in a counter clockwise direction with respect to the reference fixed Ecliptic (Ec_0) at Julian date J2000, the net period of precession is about 21.7 ka. The general precession in longitude ψ is thus defined by $\psi = \Lambda - \Omega$, where Ω is the longitude of the ascending node (N), and Λ the inclination of Ec_t (Fig. 1). The angle between the Earth's equatorial plane (Eq_t, Fig. 1) and Ec_t is the obliquity (ε). The current value for ε is 23.44° but it varied from about 22 to 24.5° during the past 15 Ma with a main period of about 41 ka (Fig. 2c). In the earlier episodes of Earth's history, obliquity oscillated at a much shorter period (i.e., ~29 ka at 500 Ma [37]). This is because the Earth's rate of rotation has declined with time due to tidal friction.

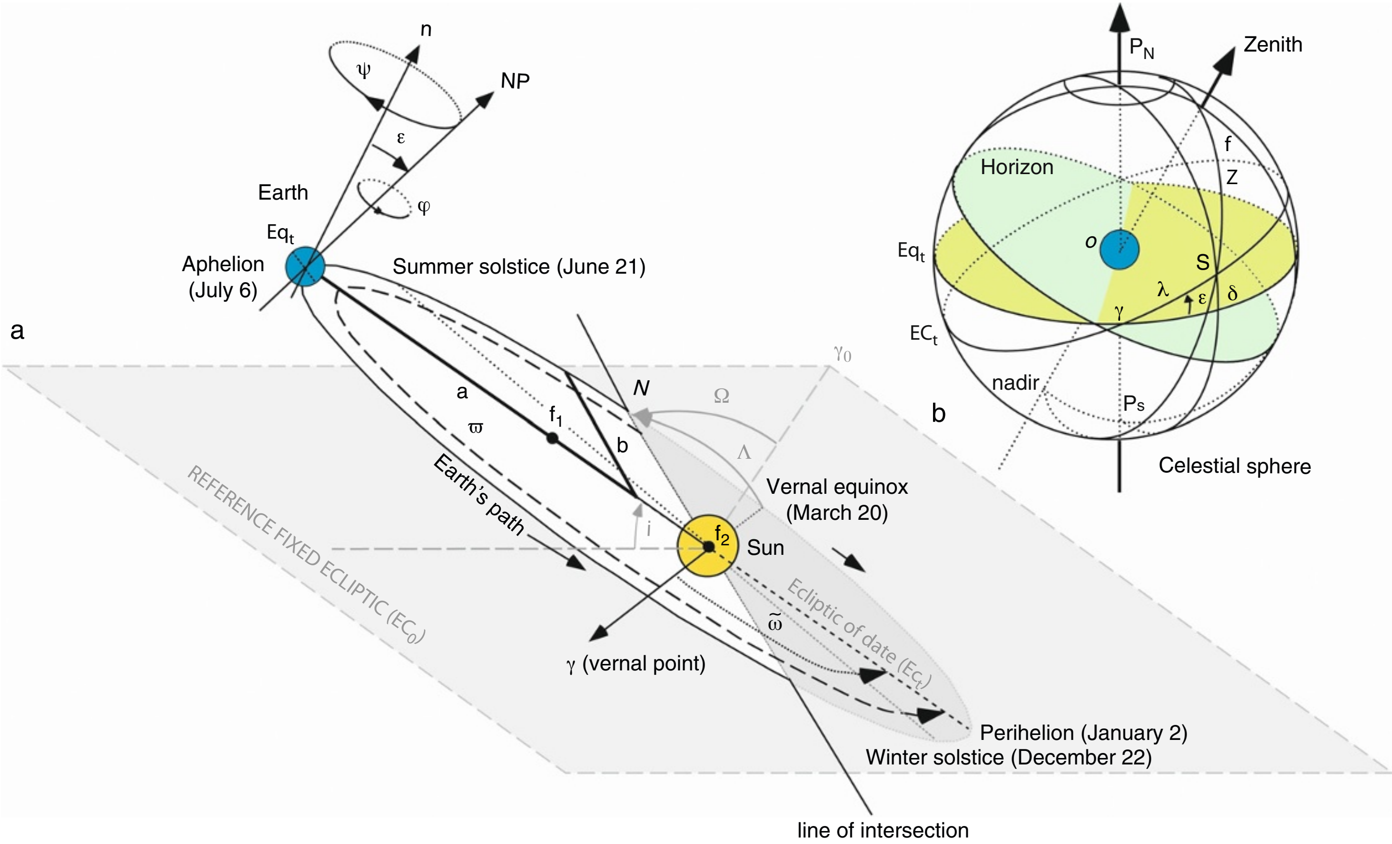

FIGURE 1 Astronomical configuration of the Earth. (a) Elements of the Earth's orbital parameters (modified after [101]). (b) Position of a point (S) on the celestial sphere (modified after [38]). See text for explanations.

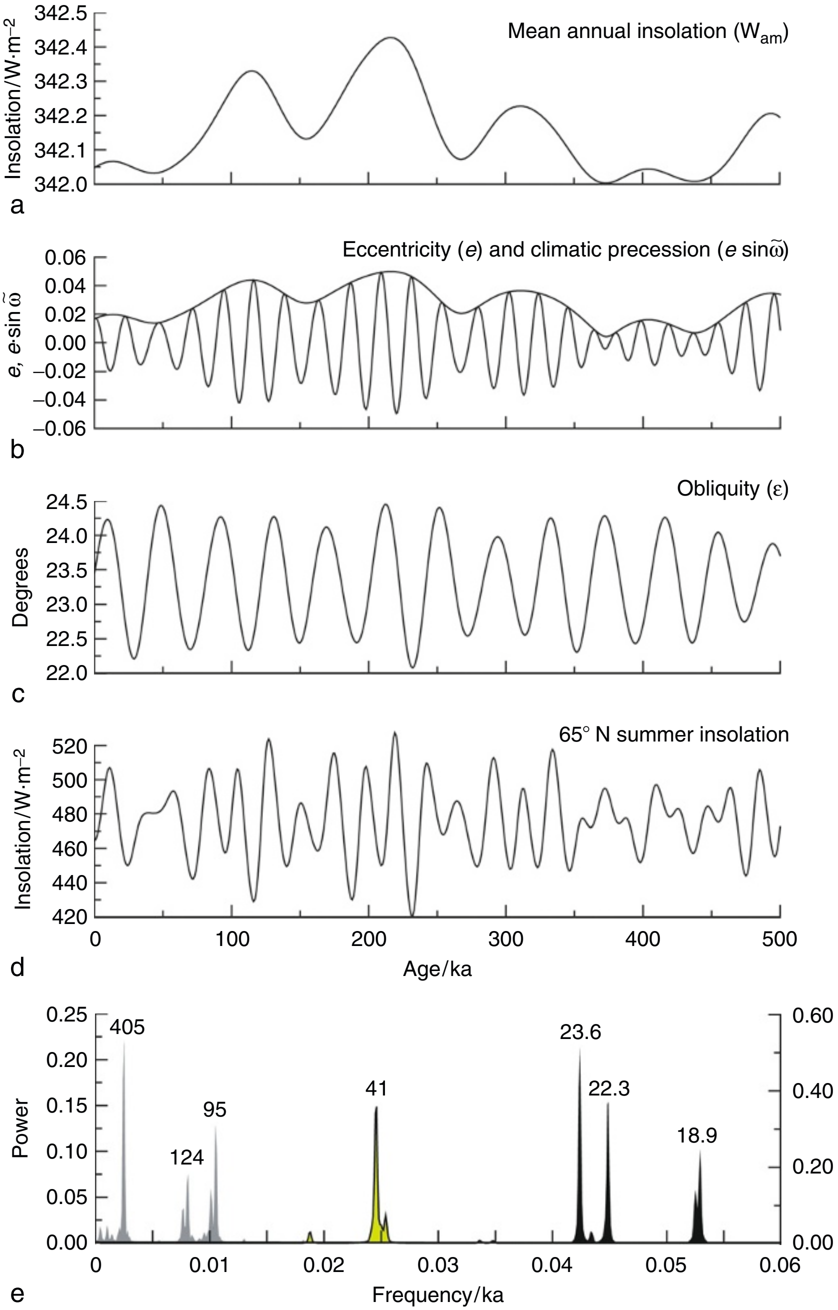

FIGURE 2 Variations of the Earth's orbital parameters over the past 500 ka according to the La04 solution [32]. (a) Mean annual insolation including a solar constant of 1368 W·m^{-2}. (b) Eccentricity (solid) and climatic precession (dotted line). (c) Obliquity. (d) 65°N summer (21 May–20 July) insolation. (e) Combined power spectrum of eccentricity (grey), obliquity (grey plus solid line) and precession (black) for the past 15 Ma.

For paleoclimate studies, the usual quantity that relates more to insolation is the climatic precession index $e \cdot \sin \overline{\varpi}$, where $\overline{\varpi} = \boldsymbol{\varpi} + \psi$. $\boldsymbol{\varpi}$ is the approximation of the longitude of perihelion of the Earth from the fixed J2000 and $\overline{\varpi}$ the resulting longitude of perihelion from the moving vernal equinox (Fig. 1a). In practice, however, the numerical calculations are done using the direction in which the Sun is seen from the Earth at the beginning of the spring, the so-called vernal point γ (Fig. 1) as reference. In most cases the climatic precession index is, therefore, given by $e \cdot \sin \tilde{\omega}$, where $\tilde{\omega} = \overline{\varpi} - 180°$ [13]. This implies that climatic precession is at a minimum when NH summer solstice is in perihelion, so that when $\tilde{\omega}$ is 270° (or $\overline{\varpi}$ is 90°).

The eccentricity term in the climatic precession index is operating as a modulator of the precession-related insolation changes (Fig. 2b). In case of a circular orbit (eccentricity is zero), perihelion is undefined and there is no climatic effect associated with precession, while in case the Earth's orbit is strongly elongated the effect of precession on insolation is at a maximum. The three most important periods of the climatic precession parameter over the past 15 Ma are about 23.6, 22.3 and 18.9 ka (Fig. 2e). Just as for obliquity, the periods of precession shorten back in time due to tidal dissipation with ~3–4 ka over the past 500 Ma [37].

2.3. Insolation

If the orbital parameters are known, the insolation for any latitude and at any time of the year can be computed. The mean annual insolation at the surface of the Earth depends only on the eccentricity and is represented by the following equation [24]:

$$W_{\mathrm{am}} = \frac{S_0}{4\sqrt{(1 - e^2)}} \tag{2}$$

S_0 is called the 'solar constant'. In fact, the intensity of the Sun varies along with the number of sunspots. Recent observations have shown that when sunspots are numerous (scarce) the solar constant is about 1368 $\mathrm{W \cdot m^{-2}}$ (1365 $\mathrm{W \cdot m^{-2}}$). In literature, the various astronomical computations include values for S_0 ranging from 1350 $\mathrm{W \cdot m^{-2}}$ [24] to 1360 $\mathrm{W \cdot m^{-2}}$ [38]. The variations in mean annual insolation are very small, as they depend on the square of the eccentricity, with the largest mean annual insolation values reached during eccentricity maxima (Fig. 2a). Orbital-induced mean annual insolation changes are, therefore, not seen as the primary cause of past climate changes. On the contrary, according to Milankovitch's theory [10] summer insolation at high northern latitudes (Fig. 2d) played in particular a crucial role on the waxing and waning of the ice sheets. The theory states that in case insolation in summer was not high enough, ice sheets could expand. It is, therefore, important to compute the daily (or monthly) insolation at any given point on the Earth.

Following Berger and Loutre [38], insolation W received on a horizontal surface at latitude ϕ and a given time (H) during the course of the year (λ) is described by:

$$W(\phi, \lambda, H) = S_0 \left(\frac{a}{r}\right)^2 \cos z \tag{3}$$

where r is the distance to the Sun and z the solar zenith angle (or zenith distance). The horizontal surface of the position of the observer (o) refers to the plane perpendicular to the direction of the local gravity, while the zenith is the point vertically upward (Fig. 1b). The zenith distance z of any point S (i.e., the position of the Sun seen in the sky from the observer at time H) on the celestial sphere is the angular distance from the zenith measured along the vertical circle through the given point (Fig. 1b). It varies from 0 to 180°.

The point S can also be calculated from the angle between the meridian (great circle through the celestial poles P_n and P_s, the zenith and the nadir) and the secondary great circle through the point and the poles (Fig. 1b). This angle is called the hour angle H. This gives the following relationship:

$$\cos z = \sin \phi \sin \delta + \cos \phi \cos \delta \cos H \tag{4}$$

The declination δ is the angular distance of point S measured from the equator on the secondary great circle. The latitude ϕ is the angular distance from the equator to the zenith measured on the meridian. The declination δ is related to the true longitude λ of the Earth by:

$$\sin \delta = \sin \lambda \sin \varepsilon \tag{5}$$

Over one year, λ varies from 0 to 360° while δ varies between $-\varepsilon$ and $+\varepsilon$. The Earth–Sun distance r is given by the ellipse equation:

$$r = \frac{a(1 - e^2)}{1 + e \cos v} \tag{6}$$

with v being the true anomaly related to the true longitude λ of the Earth by:

$$v = \lambda - \varpi \tag{7}$$

Combining Eqns (4)–(7), Eqn (3) can be rewritten as

$$W(\phi, \lambda, H) = S_0 \frac{(1 + e \cos (\lambda - \varpi))^2}{(1 - e^2)^2} (\sin \phi \sin \lambda \sin \varepsilon + \cos \phi \cos \delta \cos H) \tag{8}$$

Over one year, ε, ϖ and e are assumed to be constant. Over a given day λ and δ are assumed to be constant, while H varies from 0 at solar noon to 24 h (0–360°). The long-term behaviour of each factor in Eqn (8) is thus governed by a different orbital parameter. The obliquity ε drives $\cos z$, the precession ϖ drives $(1 + e \cos(\lambda - \varpi))^2$ and the eccentricity e drives $(1 - e^2)^{-2}$. Note that the eccentricity appears as $(1 - e^2)^{-2}$ while in the mean annual insolation it appears as $(1 - e^2)^{1/2}$ (see Eqn (2)).

To illustrate the influence of precession on insolation, we plotted the monthly averaged zonal insolation difference between a climatic precession minimum and maximum situation (Fig. 3a). This comparison shows that high northern (southern) latitudes receive (dispatch) more than 100 W·m^{-2} of additional insolation during summer (~20%) when they occur in perihelion

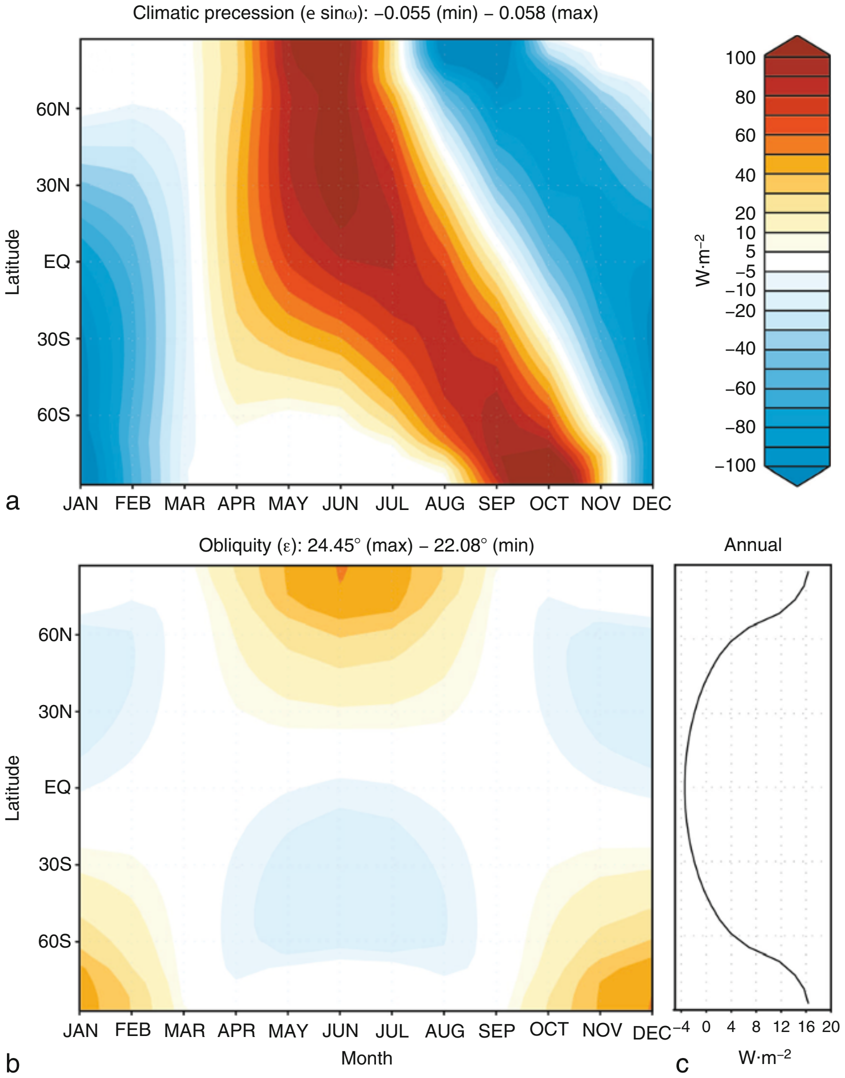
Climatic precession (e sinω): –0.055 (min) – 0.058 (max)

Obliquity (ε): 24.45° (max) – 22.08° (min)

Annual

FIGURE 3 Monthly incoming differences in W·m^{-2} at the top of the atmosphere. (a) Insolation differences between a minimum (−0.055) and a maximum (+0.058) climatic precession configuration. (b) Insolation differences between a maximum obliquity (Tilt = 24.45°) and a minimum obliquity (Tilt = 22.08°) configuration with zero eccentricity. (c) As in (b), but now plotted the annual incoming insolation differences. Solar constant = 1360 W·m^{-2}.

(aphelion). In contrast, the accompanying NH (SH) winters receive less (more) insolation. Thus during a precession minimum seasonal contrasts at the NH increase, whereas they decrease at the SH. In contrast, a change in obliquity causes a simultaneous shift in seasonal contrasts at both hemispheres (Fig. 3b). From an obliquity minimum to maximum situation high-latitudes receive more than 50 $W \cdot m^{-2}$ of additional insolation during summer, while winters gain considerable (~15 $W \cdot m^{-2}$) less insolation.

In contrast to precession, obliquity influences the mean annual insolation at certain latitude. When obliquity increases, the poles receive more energy in summer but stay in the polar night during winter. The annual mean insolation, therefore, increases symmetrically at the poles and consequently the annual insolation must decrease around the equator (Fig. 3c) because the global annual insolation does not depend on obliquity (Eqn (2)).

3. ORBITAL-INDUCED CLIMATE CHANGE

Since the pioneering work of Cesare Emiliani [39], the stable oxygen isotope ratio between ^{16}O and ^{18}O (denoted by $\delta^{18}O$) of calcareous (micro) fossil shells has been extensively studied to improve our understanding of paleoceanographic and paleoclimate changes. He used this ratio to reconstruct glacial–interglacial variations in sea water temperature over the past 500 ka. His study gave strong support to the hypothesis of Milankovitch and revolutionised ideas about the history of the oceans and the role of orbital forcing. Soon afterwards, Nick Shackleton [40] argued, however, that the isotopic signal was partly caused by ice volume changes. When ice caps grow, ^{16}O is preferentially stored on the continents resulting in heavier oxygen isotope values (^{18}O-enriched) of the ambient sea water in which the calcareous organisms thrive.

Over the past decades, the inventory of high-resolution oxygen isotope records across the Cenozoic, 0–65 Ma, has grown, because of the greater availability of high-quality sediment cores. A compilation of these records showed that global climate cooled over the past 50 Ma with maximum temperature conditions occurring between 50 and 55 Ma [1]. The first permanent ice caps start to occur on Antarctica around the Eocene-Oligocene transition, ~34 Ma. Also recently, extensive ice-rafted debris, including macroscopic dropstones, were found in the late Eocene to early Oligocene sediments from the Norwegian-Greenland Sea, indicating already severe glaciations of East Greenland at that time [41]. Orbital-induced variations in $\delta^{18}O$ were also detected superimposed on this long-term trend, but revealed different spectral characteristics pending on the background climate state. An evaluation of these characteristics with emphasis on icehouse and greenhouse conditions is given in the following sections.

3.1. Ice Ages

Through the development of radio-isotopic dating methods, power spectra could be obtained from the oxygen isotope records in the time domain. These methods clearly demonstrate that for the past 700 ka, major climate cycles have followed variations in obliquity and precession, although the dominant spectral power occurs at ∼100 ka [42,43]. Understanding the mechanisms which control this long-term variability remains an outstanding question in climate sciences [44]. The most widely adopted explanation is that it originates from a nonlinear response to the precession forcing [43,45]. Other theories relate the 100 ka glacial rhythm directly to eccentricity [46], but the insolation changes that may have caused this are probably too small to be of much climatic relevance (Fig. 2a).

A third category of theories attribute the 100 ka glaciations to an internal oscillation of the Earth's ice–atmosphere–ocean climate system [47], which is nonlinear phase-locked to the external Milankovitch forcing [48,49]. An historically important example of a nonlinear oscillator is the model of Imbrie and Imbrie [45] which may be written as:

$$\frac{\mathrm{d}V}{\mathrm{d}t} = \frac{1 \pm b}{T_\mathrm{m}}(X - V) \tag{9}$$

where X is the model's forcing function (i.e., the 65°N summer insolation), T_m is a mean time constant of the ice sheet response and b a nonlinearity coefficient which switches sign depending on whether ice volume is increasing or decreasing. For the late Pleistocene a T_m of 17 ka and b of 0.6 were estimated, which result in a 4–5 ka lag (ice-sheet response time) for the precession components and an 8 ka lag for obliquity [50]. In the latest marine benthic oxygen isotope stack of Lisiecki and Raymo [51], the same model has been applied. A plot of the LR04 record for the last 350 000 a is presented as overlay of the model's output in Fig. 4a. Evidently, changes in the marine δ^{18}O record lag 65°N summer insolation (Fig. 4d) with a few thousands of years as a result of the adopted values for T_m and b. The δ^{18}O record, however, preserves not only an ice volume signal, but also a deep-water temperature component, which should be taken into account for a more accurate estimate of the δ^{18}O response to orbital forcing [52].

Using an inverse modelling technique, Bintanja and coworkers [53] seperated the LR04 δ^{18}O record into an ice volume and a temperature component. The ice volume component is expressed in terms of sea level equivalent (Fig. 4b), while the temperature component is translated into the annual surface air temperature (T_air) over the continents north of 40°N (Fig. 4c). Clearly, T_air leads ice volume increases up to a few thousands of years, because ice sheets will only start to grow (inception) below a certain temperature threshold (−5 °C), and they can not expand faster than the rate at which mass is gained through snow accumulation [53]. During deglaciations, surface air temperature and sea-level increase almost in-concurrence, presumably the result of the rapid melt-down of the large ice sheets, with sea-level rises of over 1.5 $\mathrm{cm \cdot a^{-1}}$ during the major terminations $T_\mathrm{I–IV}$ (Fig. 4b).

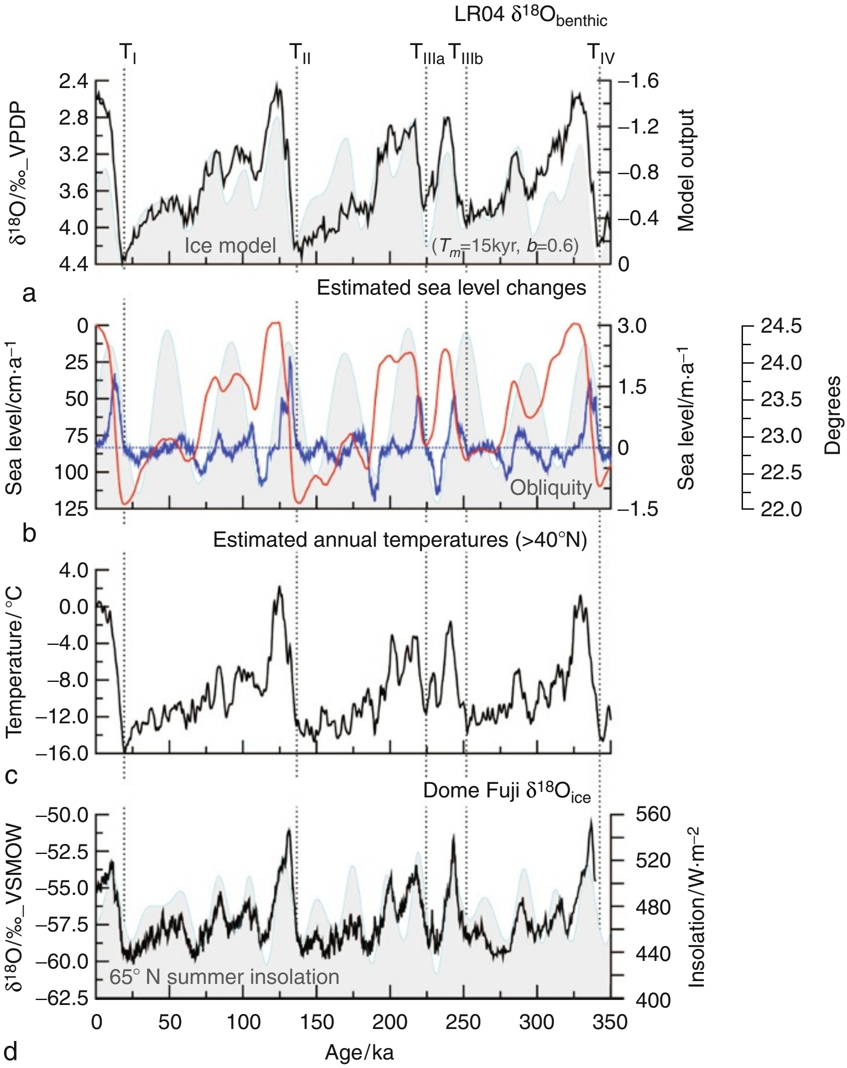

FIGURE 4 Comparison between orbital cycles and climatic proxy records for the past 350 ka (late Pleistocene). (a) LR04 δ^{18}O benthic stacked record (solid) plotted as overlay to its tuning target, represented by the outcome (thin line and grey area) of simple ice sheet model [45] including a mean time constant of the ice sheet response (T_m) of 15 ka and a nonlinearity coefficient (b) of 0.6 and the 65°N summer insolation as input [51]. (b) Reconstructed global sea level (thin line) and sea level change (solid line) derived from the LR04 δ^{18}O benthic stacked record and the use of an inverse modelling technique [53]. On the background (grey) is plotted the obliquity time series. Major terminations (I–IV) are defined by the first increase in sea level at the end of the glaciations. (c) The modelled surface air temperature deviation from present (mean over the continents between 40°N and 80°N) [53]. (d) Dome Fuji $\delta^{18}O_{ice}$ (solid) as overlay to the 65°N summer insolation curve [54].

The estimated T_{air} component of the marine $\delta^{18}O$ record resembles the Antarctic $\delta^{18}O_{\mathrm{ice}}$ record of Dome Fuji [54], although the latter record tend to lead T_{air} in the order of a few thousands of years (Fig. 4d). There are several explanations which may account for the discrepancy between the insolation-induced response times of T_{air} and the Antarctic $\delta^{18}O_{\mathrm{ice}}$ record. First of all, the $\delta^{18}O_{\mathrm{ice}}$ record depends, besides local temperature, on a variety of factors such as sea water $\delta^{18}O$ and the temperature of the water vapour source area. A reconstruction of the $\delta^{18}O_{\mathrm{ice}}$-derived local temperatures showed for example a slightly larger response time, of ~2 ka, to the insolation forcing [54].

Another part of the discrepancy may arise from uncertainties in the chronologies of either Dome Fuji or the LR04 $\delta^{18}O$ record. It should be noted that the LR04 $\delta^{18}O$ chronology is not directly constraint by radio-isotopic measurements of the marine cores that were incorporated in the LR04 stack, but it relies on the correlation between Thorium-230 and Protactinium-231 dated sea level reconstructions from coral terraces [55–58] and their signature in the $\delta^{18}O$ record, where no distinction has been made between the temperature and ice volume contribution of the $\delta^{18}O$ signal. Although the chronology of the last glacial cycles is well constraint there are conflicting estimates for the age of the penultimate and earlier deglaciations, which argue for [59] and against [60–62] the Milankovitch theory.

The Dome Fuji chronology, on the other hand, is based on tuning of the O_2/N_2 ratio of the trapped ice to the local variations in summer insolation (21 December at 77°S). The O_2/N_2 ratio lacks a strong 100 ka response, which makes this proxy more suitable for tuning than the $\delta^{18}O_{\mathrm{atm}}$ record applied previously by Shackleton [52]. Dating uncertainties in this time scale range from 0.8 to 2.9 ka at the tie points [54]. Given these uncertainties, the increases in Antarctic temperature and atmospheric carbon dioxide concentration coincide with the rising phase of NH summer insolation during the last four terminations (Fig. 4d), thereby supporting the Milankovitch theory [54].

The role of obliquity is less highlighted in glacial theories despite the fact that from about 1 to 3 Ma and also during older geological periods, such as the Middle Miocene (14–15 Ma), smaller ice sheets varied at an almost metronomic 41 ka rhythm [63–66]. There are several mechanism proposed to explain the obliquity-dominated climate cycles (Fig. 5a). The most straightforward possibility is that because high-latitude (annual and summer) insolation declines with a reduced tilt of the Earth's axis (Figs. 3b and c), the ice caps will grow, Earth's albedo increases, and global mean temperatures decrease [10]. Another possibility is that during obliquity minima the meridional gradient of insolation during the summer half-year of both hemispheres increases, causing an increased moisture transport to the poles and hence the buildup of large ice caps [67]. Evidently, most periods of maximum sea level lowering or ice-sheet growth over the past 350 ka occur during obliquity minima (Fig. 4). In addition, Huybers and Wunsch [68] presented simple stochastic and deterministic models that describe the timing of the late Pleistocene glacial

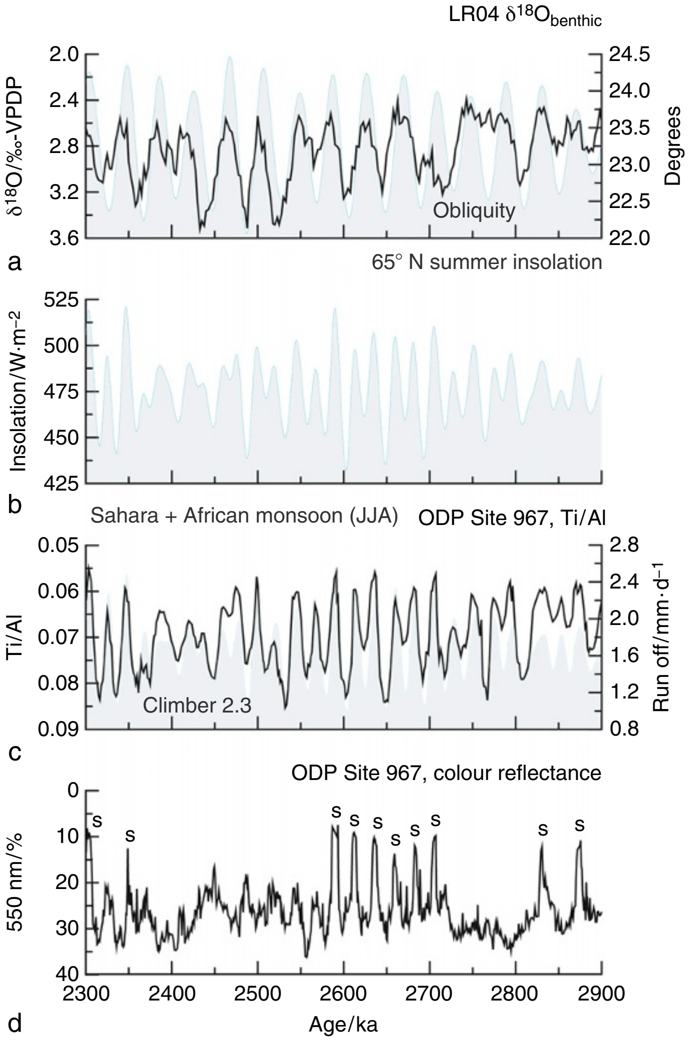

FIGURE 5 Comparison between orbital cycles and climatic proxy records for the late Pliocene time interval (2.3–2.9 Ma). (a) LR04 $\delta^{18}O$ benthic stacked record (solid) [51] plotted as overlay to the obliquity time series (thin line and grey area). (b) The 65°N summer insolation curve. (c) Reconstructed Ti/Al ratio of ODP Site 967 (solid) [31,102] as overlay to our modelled (see text for explanations) runoff associated with the Sahara and the African monsoon (blue line and grey area). (d) Colour reflectance data of ODP Site 967 (solid). Sapropels (s) are marked by very low (dark) values.

terminations purely in terms of obliquity forcing, although their findings were not yet confirmed by for instance the new results of Dome Fuji [54].

To summarise, the development of glacial-independent chronologies has become one of the major challenges in climate sciences to further unravel the Milankovitch theory of the Ice Ages. These chronologies could provide new insights to key issues such as the phase relation between climate change and the atmospheric carbon dioxide concentration, the feedback mechanisms associated with the buildup of large icecaps, or whether terminations are caused by internal or external processes.

3.2. Low and Mid-Latitude Climate Changes

The expression of orbital-induced climate oscillations is not restricted to glacial–interglacial variability. Data and models revealed that climate variations in the low and mid-latitudes are dominated by the precession cycle [69–73]. For instance, high-resolution absolute-dated oxygen isotope records from speleothems of central China have provided insights into the factors that control the strength of the East Asian Monsoon for the past 224 ka [74]. The record is dominated by precession cyclicity that is synchronous within dating errors with NH summer insolation. This supports the idea that on orbital timescales (sub)tropical monsoons respond dominantly and instantly to changes in NH summer insolation.

Another example is the cyclic occurrence of sapropels (organic-rich layers) in the marine sediments of the Mediterranean throughout the last 13 Ma [33,75]. The underlying mechanism that caused their formation gave rise to a contentious debate over the relative importance of anoxia caused by stable stratification [76] versus productivity [77]. The stratification hypothesis links the reduced oxygen conditions of the deep waters during sapropel formation to a weaker thermohaline circulation caused by lowered surface water density conditions in the eastern Mediterranean. Rossignol-Strick [78] proposed that these circumstances were triggered by the enhanced discharge of the river Nile during precession minima (NH summer insolation maxima, Fig. 2) when the strength of the African monsoon is at a maximum [70]. Climate modelling experiments, including a regional ocean model for the Mediterranean Sea, revealed however, that the precession-induced increase in net precipitation over the Mediterranean Sea itself is of equal or greater importance than the increase in runoff from the bordering continents [79]. Evidence for enhanced primary productivity has been gathered by a variety of geochemical and micropaleontological proxy records [77,80–84]. As possible causes for the enhanced nutrient supply to the mixed layer has been proposed a reversal in the flow directions of the nutrient-poor surface and nutrient-enriched deep waters, increased runoff, and the development of a Deep Chlorophyll Maximum (DCM).

To illustrate the different orbital characteristics of low and high-latitude driven climate signals a comparison is shown between the open ocean LR04 $\delta^{18}O$ record and the sapropel patterns of ODP (Ocean Drilling Program) Site 967 (Eratosthenes Seamount, eastern Mediterranean) for the time interval between 2.3 and 2.9 Ma are shown in Figs. 5a and d, respectively. Obliquity dominates the globally recorded high-latitude driven glacial–interglacial oscillations, whereas the climatic precession determines the circum-Mediterranean climate variability. The sapropels do not occur during all NH summer insolation maxima, indicating that their formation is bound to a threshold in the ocean–climate system. From the same core, changes in the Titanium to Aluminum ratio (Ti/Al), however, do show a striking correspondence with 65°N summer insolation throughout the studied interval, where high (low) Ti/Al values are interpreted to reflect a relative larger (lower) contribution of wind-blown (e.g., Sahara dust) versus river-transported (e.g., by the river Nile) derived terrigenous material [31] (Fig. 5c). Clearly, changes in northern African aridity conditions respond almost linearly to the orbital forcing, that is, containing both an obliquity and a precession signal.

To further unravel the link between the Ti/Al index and northern African aridity we simulated changes in runoff derived from the northern part of the African continent using an atmosphere–ocean–vegetation model of intermediate complexity, CLIMBER-2.3 [85]. The atmospheric model is a statistical–dynamical model with a resolution of 10° in latitude and ~51° in longitude. The terrestrial vegetation model, VECODE (VEgetation COntinuous Description), computes the fraction of the potential vegetation (i.e., grass, trees and bare soil) from the annual sum of positive day-temperatures and the annual precipitation [86]. These vegetation changes affect the land-surface albedo and the hydrological cycle. The ocean model [87] computes the zonally averaged temperature, salinity and velocity for three separate basins (Atlantic, Indian and Pacific oceans). The latitudinal resolution is 2.5° and the vertical resolution is 20 unequal levels. We have run a transient simulation for the time-interval between 2.25 and 3.0 Ma in which the only forcing is variations in insolation induced by the orbital parameters. Boundary conditions like orography, land–sea configuration, ice sheets and concentration of trace gasses were kept constant at pre-industrial values. As an indicator for northern African aridity, we extracted the total amount of runoff for the months June, July and August of the Sahara (20°N–30°N, 11°W–40°E) and African monsoon (10°N–20°N, 11°W–40°E) grid boxes [88]. This transient experiment shows that within a precession period runoff fluctuated between 1 and 2.6 $\text{mm}\cdot\text{d}^{-1}$, with the lowest values being associated with minima in 65°N summer insolation (Figs. 5b and c). The Ti/Al record and the modelled runoff shows a very good similarity revealing that the Ti/Al index reflects northern African aridity.

Spectral analyses of the Ti/Al index and simulated runoff show that African runoff is determined by precession and obliquity of which the first dominates the signal. Similar results have been found using several generic radiation patterns with an AGCM (Atmospheric General Circulation Model) in permanent July mode [89] or with time slice experiments of orbital extremes using the intermediate complexity model ECBilt [90]. These experiments show that during precession minimum or obliquity maximum configurations the African monsoon intensifies and extends further northwards.

In, contrast to obliquity, precession also influences the seasonal timing of the occurrence of the maximum precipitation [90]. The influence of obliquity could be due to stronger wind from the Atlantic Ocean into southern North Africa forced by deepening of the convergence zone over southern Asia during maximum summer insolation at high latitudes.

As for the origin of Ice Ages and the timing of major terminations, uncertainties exist in our knowledge of the exact phase relation between astronomical forcing and low-latitude climate changes. Where most model experiments suggest that tropical monsoons respond instantly to changes in NH summer insolation [70,71,88], reconstructions of Indian monsoon variability from the Arabian Sea have proposed a long response time of up to 8.0 ka after the inferred precession minimum configuration [91–95]. Also radiometric dates of the youngest sapropel in the Mediterranean (S1) suggest a time lag of ~3.0 ka between the last precession minimum at 11.5 ka and the midpoint of the S1 dated at 8.5 ka [30]. The Chinese speleothem records, on the other hand, support an in-phase relationship of the East-Asian summer monsoon with NH July insolation [74]. Several scenarios have been proposed to explain the long phase lag of the marine records, ranging from the influence of glacial–interglacial variability on the monsoon to a SH forcing through latent heat transport [92].

3.3. Greenhouse World

During the late Oligocene and early Miocene (~18–27 Ma), when the Polar regions were only partially ice-covered, benthic isotope records exhibit, besides a dominant obliquity component, a strong response to eccentricity forcing [96]. In the absence of permanent ice caps between 35 and 65 Ma, the imprint of eccentricity seems even more prominent, although the benthic isotope records currently available for the early Cenozoic lack adequate resolution to fully characterise obliquity variance [1]. The pronounced eccentricity imprint can be explained by filtering effects of the precession forcing due to continental geography and differences in land–sea heating, especially in the tropics [73]. A variety of processes have been suggested for exporting the signals to higher latitudes, including changes in ocean and atmospheric circulation, heat-transport, precipitation or the global carbon cycle and pCO2. Evidence of changes in the carbon cycle are given for instance by the Oligocene–Miocene carbon isotope (δ^{13}C) records, which exhibit pervasive large-amplitude 100 and 400 ka oscillations that are highly coherent with the benthic oxygen isotope records [96,97].

Also during the late Paleocene and early Eocene (~60–50 Ma), eccentricity has significantly modulated the carbon isotope records of the Atlantic and Pacific oceans [98]. Cramer and coworkers [98] identified several short-lived δ^{13}C depletions, which they linked to maxima in the Earth's orbital eccentricity cycle. They linked, however, the much larger Carbon Isotope Excursion (CIE) that marks the Paleocene/Eocene boundary to a minimum in the

400 ka eccentricity cycle, thereby excluding orbital-forcing as triggering mechanism for the Paleocene/Eocene Thermal Maximum (PETM). This is in contrast to the more recent findings of Lourens and coworkers [34], showing on basis of the more complete successions from the southern Atlantic Walvis Ridge depth transect [99] that the PETM and Eocene Thermal Maximum 2 do correspond to 400 and 100 ka eccentricity maxima. They suggested that the critical conjunction of short, long and very long eccentricity cycles and the long-term late Palaeocene to early Eocene warming trend may have favoured the build-up of a significant methane hydrate reservoir before its release during both hyperthermal events.

Although the proposed orbital control as forcing mechanism of Paleogene hyperthermal events should be confirmed, it is evident that eccentricity has left its mark on the global carbon cycle. Moreover, the appearance of this modulation became more visible in the geological archives when the impact of the obliquity-dominated glacial cycles is at a minimum. Evidence that these long-term changes in the carbon cycle determined global climate has not yet been solved. In particular, cross-spectral comparison between the Oligocene–Miocene $\delta^{18}O$ and $\delta^{13}C$ records revealed a time lag of more than 20 ka in the 405 ka eccentricity band, suggesting a response rather than a forcing to global climate change [96]. In addition, the conspicuous absence of the long eccentricity signal in the Pleistocene glacial cyclicity raised the so-called '400 ka problem' [45]. On the other hand, the covariance between light $\delta^{13}C$ values and severe dissolution horizons in the deep sea during the greenhouse conditions of the late Paleocene and early Eocene indicate that changes in the carbon cycle through orbital forcing has had an important impact on ocean acidification and the position of the lysocline and calcite compensation depth [100].

4. CONCLUSION

The role of orbital forcing in climate change has been unequivocally shown by their characteristic patterns in sedimentary archives, ice cores and proxy records. Although our knowledge of orbital forcing is concerned with long-term natural climate cycles, it is of fundamental importance to assess and remediate global climate change problems on short-term periods. In particular, the integration of climate modelling experiments with geological observations will provide these insights required for a better understanding of climate change in the past and near future. Considerable challenges will have to be addressed before the full spectrum of orbital-induced climatic variability has been unravelled, including the phase behaviour of different parts of the climate system, feedback mechanisms and the impact on ecosystem dynamics.

From all the evidence, it is most likely that the climate change that we are currently experiencing is not due to variations of the Earth's orbital movements. With the fast rising CO_2 concentrations in the atmosphere, general orbital theories dealing with the icehouse world conditions will probably not account for future predictions. Integrating our knowledge of geological times when greenhouse gas conditions were those as being predicted, we might be able to decipher the role of orbital forcing in future climate change scenarios.

REFERENCES

1. J.C. Zachos, M. Pagani, L. Sloan, E. Thomas, K. Billups, Science 292 (2001) 686–693.
2. J.L. Lagrange, Memoirs of Berlin Academy, Oeuvre complètes t. V, vol. 1781, Gauthier-Villars, Paris, 1870, 125–207.
3. J.L. Lagrange, Memoirs of Berlin Academy, Oeuvre complètes t. V, vol. 1782, Gauthier-Villars, Paris, 1870, 211–344.
4. G.D. Pontécoulant, Théorie Analytique of Système of Monde, t III, Bachelier, Paris, 1834.
5. L. Agassiz, Étude sur les glacier, Neuchâtel (1840).
6. J.A. Adhémar, Révolutions de la mer, privately published, Paris, 1842.
7. U. Le Verrier, Ann. Obs. Paris II, Mallet-Bachelet, Paris, 1856.
8. J. Croll, Philos. Mag. 28 (1864) 121–137.
9. L. Pilgrim, Versuch einer rechnerischen Behandlung des Eiszeitproblems. Jahreshefte des Vereins für vaterländische Naturkunde in Württemberg, Stuttgart 60: 26–117 (1904).
10. M. Milankovitch, R. Serb. Acad. Spec. Publ. 133 (1941) 1–633.
11. P. Bretagnon, Astron. Astrophys. 30 (1974) 141–154.
12. A. Berger, Astron. Astrophys. 51 (1976) 127–135.
13. A. Berger, J. Atmos. Sci. 35 (1978) 2362–2367.
14. S.G. Sharav, N.A. Boudnikova, Bull. I.T.A XI-4(127) (1967) 231–265.
15. S.G. Sharav, N.A. Boudnikova, Trud. I.T.A XIV (1967) 48–84.
16. J. Laskar, Théorie générale planétaire: Eléments orbitaux des planètes sur 1 million d'années, Thèse, Observatoire de Paris (1984).
17. J. Laskar, Astron. Astrophys. 144 (1985) 133–146.
18. J. Laskar, Astron. Astrophys. 157 (1986) 59–70.
19. J. Laskar, Astron. Astrophys. 198 (1988) 341–362.
20. J. Laskar, Nature 338 (1989) 237–238.
21. J. Laskar, Icarus 88 (1990) 266–291.
22. J. Laskar, Philos. Trans. R. Soc. Lond. A 357 (1999) 1735–1759.
23. T.R. Quinn, S. Tremaine, M. Duncan, Astron. J. 101 (1991) 2287–2305.
24. J. Laskar, F. Joutel, F. Boudin, Astron. Astrophys. 270 (1993) 522–533.
25. K. Lambeck, The earth's variable rotation: Geophysical causes and consequences, Cambridge University Press, 458 p. (1980).
26. W.R. Peltier, X. Jiang, Geophys. Res. Lett. 21 (1994) 2299–2302.
27. J.X. Mitrovica, A.M. Forte, Geophys. J. Int. 121 (1995) 21–32.
28. J.X. Mitrovica, A.M. Forte, R. Pan, Geophys. J. Int. 128 (1997) 270–284.
29. A.M. Forte, J.X. Mitrovica, Nature 390 (1997) 676–680.
30. L.J. Lourens, A. Antonarakou, F.J. Hilgen, A.A.M.v. Hoof, C. Vergnaud-Grazzini, W.J. Zachariasse, Paleoceanography 11 (1996) 391–413.
31. L.J. Lourens, R. Wehausen, H.J. Brumsack, Nature 409 (2001) 1029–1032.
32. J. Laskar, P. Robutel, F. Joutel, M. Gastineau, A.C.M. Correia, B. Levrard, Astron. Astrophys. 428 (2004) 261–285.
33. L.J. Lourens, F.J. Hilgen, N.J. Shackleton, J. Laskar, D. Wilson, in: F. Gradstein, J. Ogg, A. Smith (Eds.), A Geologic Time Scale 2004, Cambridge University Press, UK, 2004, pp. 409–440.

34. L.J. Lourens, A. Sluijs, D. Kroon, J.C. Zachos, E. Thomas, U. Röhl, J. Bowles, I. Raffi, Nature 435 (2005) 1083–1087.
35. T. Westerhold, U. Rohl, J. Laskar, I. Raffi, J. Bowles, L.J. Lourens, J.C. Zachos, Paleoceanography 22 (2007) doi:10.1029/2006PA001322.
36. K.F. Kuiper, A. Deino, F.J. Hilgen, W. Krijgsman, P.R. Renne, J.R. Wijbrans, Science 320 (2008) 500–504.
37. A. Berger, M.F. Loutre, J. Laskar, Science 255 (1992) 560–565.
38. A. Berger, M.F. Loutre, in: J.-C. Duplessy, M.-T. Spyridakis (Eds.), Long-Term Climatic Variations, vol. I22, Springer-Verlag, Berlin Heidelberg, 1994, pp. 107–151.
39. C. Emiliani, J. Geol. 63 (1955) 538–578.
40. N.J. Shackleton, Nature 215 (1967) 15–17.
41. J.S. Eldrett, I.C. Harding, P.A. Wilson, E. Butler, A.P. Roberts, Nature 446 (2007) 176–179.
42. J.D. Hays, J. Imbrie, N.J. Shackleton, Science 194 (1976) 1121–1132.
43. J. Imbrie, A. Berger, E.A. Boyle, S.C. Clemens, A. Duffy, W.R. Howard, G. Kukla, J. Kutzbach, D.G. Martinson, A. McIntyre, A. Mix, B. Molfino, J.J. Morley, L.C. Peterson, N.G. Pisias, W.L. Prell, M.E. Raymo, N.J. Shackleton, J.R. Toggweiler, Paleoceanography 8 (1993) 699–735.
44. B. Saltzman, Dynamical Paleoclimatology: Generalised Theory of Global Climate Change, vol. 80, Elsevier, New York, 2001, pp. 320.
45. J. Imbrie, J.Z. Imbrie, Science 207 (1980) 943–952.
46. R. Benzi, G. Parisi, A. Sutera, A. Vulpiani, Tellus 34 (1982) 10–16.
47. H. Gildor, E. Tziperman, Paleoceanography 15 (2000) 605–615.
48. K.A. Maasch, B. Saltzman, J. Geophys. Res. 95 (1990) 1955–1963.
49. E. Tziperman, M.E. Raymo, P. Huybers, C. Wunsch, Paleoceanography 21 (2006) PA4206.
50. J. Imbrie, J.D. Hays, D.G. Martinson, A. McIntyre, A.C. Mix, J.J. Morley, N.G. Pisias, W.L. Prell, N.J. Shackleton, in: A. Berger, J. Imbrie, J. Hays, G. Kukla, B. Saltzman (Eds.), Milankovitch and Climate, Understanding the Response to Astronomical Forcing, Part I, D. Reidel Publishing Company, Dordrecht/Boston/Lancaster, 1984, pp. 269–305.
51. L.E. Lisiecki, M.E. Raymo, Paleoceanography 20 (2005) PA1003.
52. N.J. Shackleton, Science 289 (2000) 1897–1902.
53. R. Bintanja, R.S.W.v.d. Wal, J. Oerlemans, Nature 437 (2005) 125–128.
54. K. Kawamura, F. Parrenin, L.E. Lisiecki, R. Uemura, F. Vimeux, J.P. Severinghaus, M.A. Hutterli, T. Nakazawa, S. Aoki, J. Jouzel, M.E. Raymo, K. Matsumoto, H. Nakata, H. Motoyama, S. Fujita, K. Goto-Azuma, Y. Fujii, O. Watanabe, Nature 448 (2007) 912–916.
55. W. Broecker, D.L. Thurber, J. Goddard, T.L. Ku, R.K. Matthews, K.J. Mesolella, Science 159 (1968) 297–300.
56. R.L. Edwards, J.H. Chen, T.-L. Ku, G.J. Wasserburg, Science 236 (1987) 1547–1553.
57. R.L. Edwards, H. Cheng, M.T. Murrell, S.J. Goldstein, Science 276 (1997) 782–786.
58. E. Bard, B. Hamelin, R.G. Fairbanks, Nature 346 (1990) 456–458.
59. T.D. Herbert, J.D. Schuffert, D. Andreasen, L. Heusser, M. Lyle, A. Mix, A.C. Ravelo, L.D. Stott, J.C. Herguera, Science 293 (2001) 71–76.
60. G.M. Henderson, N.C. Slowey, Nature 404 (2000) 61–66.
61. C.D. Gallup, H. Cheng, F.W. Taylor, R.L. Edward, Science 295 (2002) 310–313.
62. I.J. Winograd, J.M. Landwehr, K.R. Ludwig, T.B. Coplen, A.C. Riggs. Q. Res. 48 (1997) 141–154.
63. N.J. Shackleton, J. Backman, H. Zimmerman, D.V. Kent, M.A. Hall, D.G. Roberts, D. Schitker, J. Baldauf, Nature 307 (1984) 620–623.
64. W.F. Ruddiman, M.E. Raymo, D.G. Martinson, B.M. Clement, J. Backman, Paleoceanography 4 (1989) 353–412.

65. M.E. Raymo, W.F. Ruddiman, J. Backman, B.M. Clement, D.G. Martinson, Paleoceanography 4 (1989) 413–446.
66. A. Holbourn, W. Kuhnt, M. Schulz, H. Erlenkeuser, Nature 438 (2005) 483–487.
67. M.E. Raymo, K. Nisancioglu, Paleoceanography 18 (2003) doi:10.1029/2002PA000791.
68. P. Huybers, C. Wunsch, Nature 434 (2005) 491–494.
69. E.M. Pokras, A.C. Mix, Nature 326 (1987) 486–487.
70. J.E. Kutzbach, Science 214 (1981) 59–61.
71. J.E. Kutzbach, X. Liu, Z. Liu, G. Chen, Clim. Dyn. 30 (2008) 567–579.
72. D.A. Short, J.G. Mengel, Nature 323 (1986) 48–50.
73. D.A. Short, J.G. Mengel, T.J. Crowley, W.T. Hyde, G.R. North, Q. Res. 35 (1991) 157–173.
74. Y. Wang, H. Cheng, R.L. Edwards, X. Kong, X. Shao, S. Chen, J. Wu, X. Jiang, X. Wang, Z. An, Nature (2008), 451, 1090.
75. F. Hilgen, Newslett. Stratigr. 17 (1987) 109–127.
76. E. Olausson, Reports of the Swedish Deep Sea Expedition 1947–1948, vol. 8, 1961, pp. 353–391.
77. S.E. Calvert, Oceanol. Acta 6 (1983) 255–267.
78. M. Rossignol-Strick, Nature 304 (1983) 46–49.
79. P.T. Meijer, E. Tuenter, J. Mar. Syst. 68 (2007) 349–365.
80. E.J. Rohling, W.W.C. Gieskes, Paleoceanography 5 (1989) 531–545.
81. D. Castradori, Paleoceanography 8 (1993) 459–471.
82. J.P. Sachs, D.J. Repeta, Science 286 (1999) 2485–2488.
83. A.E.S. Kemp, R.B. Pearce, I. Koizumi, J. Pike, S. Jea Rance, Nature 398 (1999) 57–61.
84. S.J. Schenau, A. Antonarakou, F.J. Hilgen, L.J. Lourens, I.A. Nijenhuis, C.H. van der Weijden, W.J. Zachariasse, Mar. Geol. 153 (1999) 117–135.
85. V. Petoukhov, A. Ganopolski, V. Brovkin, M. Claussen, A. Eliseev, C. Kubatzki, S. Rahmstorf, Clim. Dyn. 16 (2001) 1–17.
86. V. Brovkin, A. Ganopolski, Y. Svirezhev, Ecol. Modell. 101 (1997) 251–261.
87. T.F. Stocker, L.A. Mysak, Clim. Change 20 (1992) 227–250.
88. E. Tuenter, S.L. Weber, F.J. Hilgen, L.J. Lourens, A. Ganopolski, Clim. Dyn. 24 (2005) 279–295.
89. W.L. Prell, J.E. Kutzbach, J. Geophys. Res. 92 (1987) 8411–8425.
90. E. Tuenter, S.L. Weber, F.J. Hilgen, L.J. Lourens, Glob. Planet. Change 36 (2003) 219–235.
91. S. Clemens, W. Prell, D. Murray, G. Shimmield, G. Wedon, Nature 353 (1991) 720–725.
92. S.C. Clemens, D.W. Murray, W.L. Prell, Science 274 (1996) 943–948.
93. G.J. Reichart, L.J. Lourens, J.W. Zachariasse, Paleoceanography 13 (1998) 607–621.
94. M.A. Altabet, D.W. Murray, W.L. Prell, Paleoceanography 14 (1999) 732–743.
95. P. Wang, S. Clemens, L. Beaufort, P. Braconnot, G. Ganssen, Z. Jian, P. Kershaw, M. Sarnthein, Quat. Sci. Rev. 24 (2005) 595–629.
96. J.C. Zachos, N.J. Shackleton, J.S. Revenaugh, H. Pälike, B.P. Flower, Science 292 (2001) 274–278.
97. H.A. Paul, J.C. Zachos, B.P. Flower, A. Tripati, Paleoceanography 15 (2000) 471–485.
98. B.S. Cramer, J.D. Wright, D.V. Kent, M.-P. Aubry, Paleoceanography 18 (2003), doi: 10.1029/2003PA000909.
99. J.C. Zachos, D. Kroon, P. Blum, J. Bowles, P. Gaillot, T. Hasegawa, E.C. Hathorne, D.A. Hodell, D.C. Kelly, J.-H. Jung, S.M. Keller, Y.-S. Lee, D.C. Leuschner, Z. Liu, K.C. Lohmann, L. Lourens, S. Monechi, M. Nicolo, I. Raffi, C. Riesselman, U. Röhl, S.A. Schellenberg, D. Schmidt, A. Sluijs, D. Thomas, E. Thomas, H. Vallius. (2004), *Proc. ODP, Init. Repts.*, Vol. 208: College Station, TX (Ocean Drilling Program).
100. J.C. Zachos, G.R. Dickens, R.E. Zeebe, Nature 451 (2008) 279–283.
101. L. Hinnov, in: F. Gradstein, J. Ogg, A.Smith (Eds.), A Geologic Time Scale 2004, Cambridge University Press, UK, 2004, pp. 55–62.
102. R. Wehausen, H.-H. Brumsack, Mar. Geol. 153 (1999) 161–176.